Mon. Not. R. Astron. Soc. **000**, 000–000 (0000) Printed 10 August 2008 (MN LaTeX style file v1.4)

10 GHz Tenerife CMB observations at 8° resolution and their analysis using a new maximum entropy method

A.W.Jones[1], S. Hancock[1], A.N. Lasenby[1], R.D. Davies[2], C.M. Gutiérrez[3], G. Rocha[1], R.A. Watson[2,3] and R. Rebolo[3]

[1] *Mullard Radio Astronomy Observatory, Cavendish Laboratory, Madingley Road, Cambridge CB3 OHE, UK*
[2] *University of Manchester, Nuffield Radio Astronomy Laboratories, Jodrell Bank, Macclesfield, Cheshire, SK11 9DL, UK*
[3] *Instituto de Astrofísica de Canarias, 38200 La Laguna, Tenerife, Spain*

arXiv:astro-ph/9802351v1 27 Feb 1998

ABSTRACT

The complete set of data from the Tenerife 10 GHz (8° FWHM) twin-horn, drift scan experiment is described. These data are affected by both long-term atmospheric baseline drifts and short term noise. A new maximum entropy procedure, utilising the time invariance and spatial continuity of the astronomical signal, is used to achieve a clean separation of these effects from the astronomical signal, and to deconvolve the effects of the beam-switching. We use a fully positive/negative algorithm to produce two-dimensional maps of the intrinsic sky fluctuations. Known discrete sources and Galactic features are identified in the deconvolved map. The data from the 10 GHz experiment, after baseline subtraction with MEM, is then analysed using conventional techniques and new constraints on Galactic emission are made.

Key words: cosmic microwave background: methods: data analysis: Galaxy: general.

1 INTRODUCTION

Anisotropy of the cosmic microwave background (CMB) radiation provides one of the key constraints against which cosmological models can be tested. However, the detection of anisotropy at a level $\Delta T/T \sim 10^{-5}$ is a challenging observational problem. Attainment of these sensitivity levels is only possible by making differential measurements, switching between two different sky patches or by using interferometric techniques. The data from the telescope consist of the true sky brightness distribution convolved in some instrument beam, with an additional random noise contribution. Combined with the often non-uniform scan strategies of CMB experiments this makes the task of deconvolution to obtain a two-dimensional map of the intrinsic fluctuations a non-trivial proposition. Here we describe the analysis procedures that have been developed and applied to the Tenerife drift scan data (Davies *et al.* 1987, Watson *et al.* 1992, Hancock *et al.* 1994, Gutiérrez *et al.* 1997) in order to produce 2-D maps of the intrinsic fluctuations, while at the same time providing scans free from atmospheric baseline variations. Although the implementation described here is specific to the Tenerife instruments, some of the techniques are more generally applicable to other CMB data sets (see e.g. Maisinger *et al* 1997) and offer a useful means of comparing between observations from telescopes with different beam patterns and scan strategies.

In order to demonstrate the technique we consider here the analysis of the total data set from the original (FWHM$\sim$ 8°) Tenerife twin horn radiometer experiment (Davies *et al.* 1992). Although the instrument configuration differs from that of the current telescopes (Davies *et al.* 1996a) and is less sensitive to cosmological signals (Watson *et al.* 1992), this experiment has surveyed a substantial fraction of the full sky, making it interesting to attempt a 2-D mapping. While a partial analysis of a limited RA range, along a strip at Dec = +40° has been given elsewhere (Davies *et al.* 1987), we here present a thorough analysis of all of the data, covering a selection of declinations ranging from −15° to +45°. At the operating frequency of 10.4 GHz our maps will be sensitive to synchrotron and free-free emission in addition to the CMB and discrete radio sources. These maps can be used to constrain contaminating signals in higher frequency observations by virtue of the differing spectral dependencies of the CMB and the foregrounds. Testing the procedures on known structures will also give us improved confidence when analysing the higher frequency 15 and 33 GHz data to obtain 2-D maps of the CMB.

In Section 2 we present an analysis scheme utilising a maximum entropy based regularising function, to enable a clean separation of the astronomy from spurious atmospheric effects and to provide a deconvolved 2-D image of the microwave sky. In Section 3 we present details of the observations and the implementation of the algorithm. In Section 4 we test the positive/negative maximum entropy

© 0000 RAS

method with simulations of the observations. Section 5 details the application of the algorithm to the data from the Tenerife experiment. Sections 6, 7 and 8 describe the separation of cosmological and astronomical signals, the application of suitable significance tests and the interpretation and conclusions that were reached.

2 MAXIMUM ENTROPY DECONVOLUTION

In general the data from a CMB experiment will take the form of the true sky convolved with the instrumental response matrix with any baseline variations or noise terms added on. We assume that the observations obtained from a particular experiment have been integrated into discrete bins. For the i-th row and the j-th column the data, $y_i^{(j)}$, recorded by the instrument can be expressed as the instrumental response matrix $R_i^{(j)}(i',j')$ acting on the true sky $x(i',j')$:

$$y_i^{(j)} = \sum_{(i',j')} R_i^{(j)}(i',j')x(i',j') + \epsilon_i^{(j)}, \quad (1)$$

where i' and j' label the true sky row and column position respectively. The $\epsilon_i^{(j)}$ term represents a noise term, assumed to be random, uncorrelated Gaussian noise.

It is immediately clear from Equation 1 that the inversion of the data $y_i^{(j)}$ to obtain the two-dimensional sky distribution $x(i',j')$, is singular. The inverse R^{-1} of the instrumental response function does not exist, unless the telescope samples all of the modes on the sky and consequently there is a set of signals, comprising the annihilator of R, which when convolved with R gives zero. Furthermore, the presence of the noise term ϵ will effectively enlarge the annihilator of R allowing small changes in the data to produce large changes in the estimated sky signal. It is therefore necessary to use a technique that will approximate this inversion.

2.1 Positive and negative data reconstruction

The method that we adopt is based upon the Maximum Entropy Method (hereafter MEM) which is described in more detail in a companion paper (Maisinger *et al* 1997). The problem with the MEM method in its standard form is that it contains a logarithmic term that does not allow the inclusion of negative features in the data. Laue, Skilling and Staunton (1985) proposed a two channel MEM, which involved splitting the data into positive and negative features and then reconstructing each separately but not taking into account any continuity constraint between the two. This method is inappropriate for differencing experiments as the positive and negative features originate from the beam shape and not from separate sources. White and Bunn (1995) have proposed adding a constant onto the data to make it wholly positive. They use the Millimetre-wave Anisotropy Experiment (MAX) data to reconstruct a $5^\circ \times 2^\circ$ region of sky. As simulations we have performed show, this method introduces a bias towards positive (or negative if the data are inverted) reconstruction. The reason for this is that the added constant has to be small enough so that numerical errors are not introduced into the calculations but a lower constant will give less range for the reconstruction of negative features and so the most probable sky will be a more positive one. We propose a new method to overcome both of these problems.

We consider the image to be the difference between two positive, additive distributions:

$$x(\xi) = u(\xi) - v(\xi),$$

so that the expression for the cross entropy becomes:

$$S = \sum_{i',j'} \left[\psi_{i',j'} - 2m_{i',j'} - x_{i',j'} \ln \left(\frac{\psi_{i',j'} + x_{i',j'}}{2m_{i',j'}} \right) \right], \quad (2)$$

where $\psi_{i',j'} = (x_{i',j'}^2 + 4m_{i',j'}^2)^{1/2}$. The entropy term constitutes our prior information about the fluctuations and represents the minimum amount of information obtainable from the data. $m_{i',j'}$ can be considered as a level of 'damping' imposed on $x_{i',j'}$ rather than a default model as in standard MEM. A large value of m allows large noisy features to be reconstructed whereas a small value of m will not allow the final sky to deviate strongly from the zero mean. However, m does not include any correlations between pixels and so no 'smoothing scale' is introduced into the reconstruction. The final reconstruction will contain no information on small angular scales because the experiment is not sensitive to these scales and not because the MEM approach biases the data. The detailed derivation of Equation 2 can be found in Maisinger *et al.* (1997). In a Bayesian sense we have now defined our prior and we can calculate the probability of obtaining our reconstructed sky x (the hypothesis) given y (the data):

$$\Pr(x|y) \propto \Pr(x)\Pr(y|x), \quad (3)$$

We can maximise $\Pr(x|y)$ to obtain the most likely 2-D image of the microwave sky.

3 APPLICATION TO THE DATA

As a demonstration of the power of maximum entropy we will now apply it to the beam switching experiment sited at 2400m on the island of Tenerife. The old version of the instrument operated at 10.4 GHz during the years 1984-85 and is a drift scan experiment (Davies *et al.* 1992). Repeated scans were built up at a set of declinations, -17.3, -2.4, $+1.1$, $+7.3$, $+17.5$, $+27.2$, $+37.2$, $+39.4$, $+42.6$ and $+46.6$ degrees, with the deepest integrations centred on Decs $+1.1^\circ$ and $+39.4^\circ$.

Approximately half of the time was devoted to maintenance and calibration runs, while further observing time was lost due to poor weather conditions. The instrument was left running over a continuous period of up to 2×24 hours and thus a single scan contains a maximum of 2 full coverages in right ascension, with data being taken over a period of up to 3 calendar days. Data were taken by adjusting the wagging mirror to observe the chosen declination and allowing the Earth's rotation to sweep the beams in right ascension. Each wagging cycle consisted of a 4 second integration with the beams directed to the East, followed by a 4 second integration to the West. At each position the beam difference, $(T_C - T_E) \pm \sigma_E$ or $(T_W - T_C) \pm \sigma_W$ (C, E and W denote the centre, East and West beam positions respectively), and then the corresponding difference in beam difference

Table 1. Observations with the 8.3° FWHM 10.4 GHz experiment.

Declination	Number of scans	Mean scan length (hours)	RMS length (hours)
+46.6°	15	14.1	3.1
+42.6°	16	22.0	9.7
+39.4°	42	14.1	6.3
+37.2°	18	14.6	7.6
+27.2°	17	11.3	3.9
+17.5°	16	21.1	10.3
+07.3°	13	9.7	3.3
+01.1°	52	15.8	11.1
−02.4°	6	10.7	4.9
−17.3°	20	8.4	4.2

$$(T_C - \frac{1}{2}(T_E + T_W)) \pm \sigma \tag{4}$$

where $\left(\sigma = \frac{1}{2}\sqrt{\sigma_E^2 + \sigma_W^2}\right)$, were calculated. Over each 82 second cycle, containing 6 pairs of secondary differences, the second difference and its standard deviation were recorded, along with a calibration signal. The data were calibrated and edited as described in Davies *et al.* (1992), resulting in a final data set with the properties given in Table 1 which shows the declinations surveyed, the number of coverages at each declination and the mean and standard deviation of the scan lengths in hours. The data for each scan were binned in 1° intervals in RA to convert them to a more tractable form. Binning the scans reduces the effects of short term receiver and atmospheric noise, but does not affect the long term drifts seen in individual scans.

3.1 The data scans: long period baseline drifts.

As an illustration of the nature of the data, we show in Figure 1 the set of all scans for Dec = +46.6°. Immediately evident at RA ≈ 308° is the strong Galactic plane crossing with characteristic shape due to the triple beam pattern, while at RA ≈ 70° a weaker crossing can just be discerned. A constant term has been subtracted from each scan in order to bring the non-Galactic plane sections to a mean of approximately zero. However, in *e.g.* scan 5 of this set (numbered upwards from the bottom), which is shown on an increased scale in Fig. 2, a slow variation in baselevel, amplitude (peak to peak) ∼ 2 mK, is distinctly evident. As discussed in Davies *et al.* (1992), most of the scans obtained show these variations, to a greater or lesser degree, and therefore their removal is an important part of the analysis. These long period baselines vary both along a given scan and from day to day, clearly indicating that they are due in the main to atmospheric effects, with a possible contribution from diurnal variations in the ambient conditions. We note that the timescale for these baselevel variations appears to be several hours. We examine this quantitatively by calculating the transfer function of the experiment, which defines the scales of real structures on the sky to which the telescope is sensitive. Variations produced on scales other than these will be entirely the result of non-astronomical (principally atmospheric) processes and should be removed.

As the Earth rotates the beams are swept in RA over

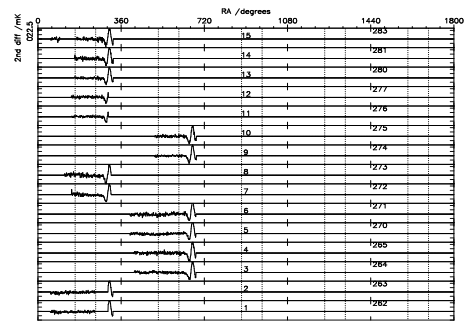

Figure 1. The 15 scans obtained at Dec = 46.6° displayed as a function of right ascension. Each plot shows the second difference in mK after binning into 1° bins. A running mean has been subtracted from each scan. Long scans are displayed modulo 360°.

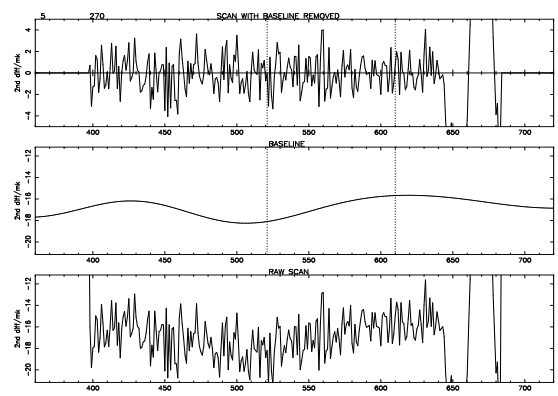

Figure 2. The data from scan 5 of Figure 1. displayed on an expanded temperature scale against RA bin number. Long timescale variations in the mean level are evident in the RAW scan (bottom panel). The middle panel shows the baseline fit found by the method of Section 2. The top panel shows the baseline corrected scan. The bin numbers exceed 360 since the scan begins near the end of an LST day, and the data are not folded modulo 360°.

a band of sky centred at a constant declination. For our present illustrative purposes, it is sufficient to approximate the beams as one-dimensional in RA, with the beam centre and the East and West throw positions lying at the same declination. The beamshape for each individual horn is well represented by a Gaussian with dispersion σ =FWHM/$2\sqrt{2\ln 2} = 3.57°$:

$$B(\theta) = \exp\left(-\frac{\theta^2}{2\sigma^2}\right), \tag{5}$$

and the beam switching in right ascension, may be expressed as a combination of delta functions:

$$S(\theta) = \delta(0) - \frac{1}{2}(\delta(\theta_b) + \delta(-\theta_b)), \tag{6}$$

for a switch angle $\theta_b = 8.3°$ in RA. So, the beam pattern is

$P(\theta) = B(\theta) * S(\theta)$.

Thus, the transfer function, (*i.e.* the Fourier transform of the beam pattern) is just:

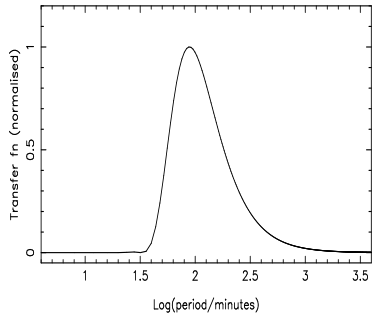

Figure 3. The transfer function for the Tenerife experiments.

$$g(k) = 2\sqrt{2\pi}\sigma \exp\left(\frac{-k^2\sigma^2}{2}\right)\sin^2\left(\frac{k\theta_b}{2}\right). \quad (7)$$

In Figure 3, the transfer function for waves of period $\theta = 2\pi/k$ is plotted. As a function of declination the θ co-ordinate must be multiplied by a factor of $\sec\delta$ because a true angle θ on the sky covers $\sim \theta/\cos\delta$ in right ascension. The peak response of the instrument is to plane waves of period $\sim 22^\circ \sec\delta$, *i.e.* individual peaks/troughs with FWHM $\sim 7^\circ$. The response drops by a factor 10 for structures with periods greater than ~ 7 hours and less than ~ 40 minutes. The long period cutoff is due to cancellation of the large-scale structures in the beam differencing pattern, while the short period cutoff is simply due to dilution of structures within a single beam. The cutoff on large scales in particular is significant for the analysis, since it tells us that variations in the data on timescales $\gtrsim 7^h \sec\delta$ are almost certainly due to long timescale atmospheric effects, or terrestrial and environmental effects, rather than being intrinsic to the astronomical sky. Thus identification and removal of such 'baseline' effects (Davies *et al.* 1992) is important. By using the whole data set to calculate the most probable astronomical sky signal with maximum entropy deconvolution, we can simultaneously fit a long-timescale Fourier component baseline to each scan. We can then stack together n days of data at a given declination to obtain a final scan with a $\sim \sqrt{n}$ improvement in sensitivity to true astronomical features.

3.2 The beam

Note that in the case of the Tenerife experiments, it is not necessary to re-define the beam matrix for each position in RA (which requires a matrix $R_i^{(j)}$ for the i-th bin in RA and j-th bin in declination) since the beam is translationally invariant in the RA direction. However, due to the large sky coverage and spherical nature of the sky it is clear that the beam shape projected into RA and Dec co-ordinates will be a function of declination. We can write the beam matrix, $R^{(j)}(i',j')$, for declination j as follows,

$$R^{(j)}(i',j') = \quad (8)$$

$$C\left[\exp\left(-\frac{\theta_C^2}{2\sigma^2}\right) - \frac{1}{2}\left(\exp\left(-\frac{\theta_E^2}{2\sigma^2}\right) + \exp\left(-\frac{\theta_W^2}{2\sigma^2}\right)\right)\right]$$

where θ_C, θ_E, and θ_W represent the true angular separation of the point (i',j') from the beam centre and the East and West throw positions respectively. The normalisation of the beam matrix is determined by C and is implemented with respect to a single beam. The angles θ_C, θ_E, and θ_W can be calculated using spherical geometry. If the beam is centred at Dec. $\delta^{(j)}$ and we let α_0 be the (arbitrary) RA origin for the definition of all the beams, for a source at a general (α,δ) corresponding to the grid point (i',j') we have a distance from the main beam centre of

$$\theta_C = \arccos\left(\sin\delta^{(j)}\sin\delta + \cos(\alpha_0-\alpha)\cos\delta^{(j)}\cos\delta\right). \quad (9)$$

There are also two other beams (with half the amplitude of the central beam), due to the beamswitching and mirror wagging, a distance θ_b (the beamthrow) either side of the central peak. These have RA centres given by the α_E or α_W in

$$\cos(\alpha_{E\,\mathrm{or}\,W} - \alpha_0) = \frac{\cos\theta_b - \sin^2\delta^{(j)}}{\cos^2\delta^{(j)}},$$

and (fairly accurately for the beamthrow used in practice) declinations of $\delta^{(j)}$ still. Thus their angular distances from the source at (i',j') can be worked out from Equation 9, yielding $\theta_{E\,\mathrm{or}\,W}$ say, and the final $R^{(j)}$ entry computed from Equation 8.

3.3 Implementation of MEM

For our data set tests have shown that we have random Gaussian noise, for which the likelihood is given by:

$$\Pr(y|x) \propto \exp\left(\frac{-\chi^2}{2}\right), \quad (10)$$

where χ^2 is the misfit statistic (Equation 15). Thus in order to maximise $\Pr(x|y)$ we simply need to minimise the function

$$F = \chi^2 - \alpha S \quad (11)$$

where we have absorbed a factor of two into the Lagrangian multiplier, α. Thus the process is to iterate to a minimum in F by consistently updating the 2-D reconstructed sky $x(i',j')$, while at the same time building up a set of baselines for each scan. The baselines are represented by a Fourier series

$$b_{ir}^{(j)} = C_{0r}^{(j)} + \sum_{n=1}^{nmax}\left[C_{nr}^{(j)}\cos(\frac{2n\pi i}{l}) + D_{nr}^{(j)}\sin(\frac{2n\pi i}{l})\right] \quad (12)$$

for the r-th scan at the j-th declination with $nmax$ baseline coefficients to be fitted. The basis data vector index i runs from 1 to 3×24^h. Thus to obtain a minimum period solution $\gtrsim 7^h \sec\delta$ (Section 3.1) we must limit the number of baseline coefficients, $nmax$ in Equation 12 to less than 9 (for the case $\delta = 40^\circ$).

For the rth scan, Equation 1 may be written

$$y_{ir}^{(j)} = y_i^{pred(j)} + b_{ir}^{(j)} + \epsilon_{ir}^{(j)}, \quad (13)$$

where the baseline variation b has now been included and

$$y_i^{pred(j)} = \sum_{i',j'} R^{(j)}(i',j')x(i'+i-i'_0,j') \quad (14)$$

is the signal we predict to be produced by the telescope in the absence of noise and baseline offsets. The beam matrix R is now defined with respect to an origin i'_o in the i' direction

as it is translationally invariant in RA. So, the χ^2 for the problem is

$$\chi^2 = \sum_{j=1}^{ndecs} \sum_{i=1}^{nra} w_i^{(j)} (y_i^{pred(j)} - y_i^{obs(j)})^2, \quad (15)$$

for a total number of declinations *ndecs*, total number of RA bins *nra* and observed data value $y_i^{obs(j)}$ with weighting factor $w_i^{(j)}$, which are a weighted average over the *ns* scans with the baseline $b_{ir}^{(j)}$ subtracted from each of the scans $y_{ir}^{(j)}$ (r is an index running over the *ns* scans). In the absence of data $w_{ir}^{(j)}$, for each individual scan, is set to zero and when data is present it is given by the inverse of the variance for the data point. It is possible to compute $y_i^{pred(j)}$, since we can use our knowledge of the geometry of the instrument to calculate the expected response function $R^{(j)}(i', j')$ for each i', j', at RA i and declination j, thus χ^2 is fully defined.

If we know the value of the regularising parameter α and the 'damping' term m then we know F and our best sky reconstruction is that for which $\partial F/\partial x_{ij} = 0$, $\forall x_{ij}$. This is most easily implemented by applying one-dimensional Newton-Raphson iteration simultaneously to each of the x_{ij} to find the zero of the function $G(x) = \partial F/\partial x$. This means that we update x from the n-th to the $(n+1)$-th iteration by

$$x_{lm}^{n+1} = x_{lm}^{n} - \gamma \left(\frac{G(x_{lm}^n)}{\left.\frac{\partial G}{\partial x_{lm}}\right|_{x_{lm}^n}} \right). \quad (16)$$

Convergence towards a global minimum is ensured by setting a suitable value for the loop gain γ and updating x_{lm} only if $\left.\frac{\partial G}{\partial x_{lm}}\right|_{x_{lm}^n}$ is positive (so that progress is always towards a minimum). By simultaneously fitting for the parameters of the baselines, it is possible to calculate the best reconstruction of the microwave sky along with an atmospheric baseline for each scan. To fit for the baseline parameters $C_{0r}^{(j)}$, $C_{nr}^{(j)}$ and $D_{nr}^{(j)}$ as expressed in Equation 12 it is sufficient to implement a simultaneous but independent χ^2 minimisation on each of these to obtain the baseline for the r-th scan. From the Bayesian viewpoint minimising χ^2 is just finding the maximum posterior probability by using a uniform prior. This is also done with a Newton-Raphson iterative technique with a new loop gain, γ_b.

3.4 Choosing alpha and m

In this MEM approach, the entropic regularising parameter α controls the competition between the requirement for a smoothly varying sky and the noisy sky imposed by our data. The larger the value of α the more the data are ignored. The smaller the value of α the more structure is reconstructed. We wish to make a choice of α that will take maximum notice of the data vectors containing information on the true sky distribution, while using the 'damping' constraint and the beam sensitivity to reject the noisy data vectors. In some sense, one may think of the entropy term as using our prior information that the sky does not contain large fluctuations at some level to fill in for the information not sampled by the response function, thereby allowing the inversion process to be implemented.

Table 2. The parameters used in the MEM inversion.

Parameter	Value
α	2×10^{-2}
m	10μK
γ	0.01
γ_b	0.05

The optimum choice of α is somewhat controversial in the Bayesian community and while several methods exist (Gull 1989, Skilling 1989) it is difficult to select one above the others that is superior. We use the criterion that $\chi^2 - \alpha S = N$, where N is the number of data points that we are trying to fit in the convolved sky. If any of the data points are weighted to zero, as the galactic plane crossing is in our case, these points should not be included in N. Increasing/decreasing α by a factor of ten decreases/increases the amplitude of the fluctuations derived in the final analysis by $\lesssim 5$ %. We decrease α in stages until $\chi^2 - \alpha S = N$; experience has shown that a convergent solution is best obtained with the typical parameter values given in Table 2 for the data set considered here. Below this value for α the noisy features in the data have a large effect and the scans are poorly fitted. Note that one cannot attach any significance to the absolute value of α, since it is a parameter that depends on the scaling of the problem.

There is less constraint on the choice of m, the 'damping' term. We choose m to be of similar size to the *rms* of the fluctuations so that the algorithm has enough freedom to reconstruct the expected features. Increasing/decreasing m by an a few orders of magnitude from this value does not alter the final result significantly so that the absolute value of m is not important. This is different to a positive only MEM because in that case m is chosen to be the default model (the value of the sky reconstruction in the absence of data) and is therefore more constrained by the problem itself. In our case as m is the default model on the two channels and not on the final sky there is a greater freedom in its choice.

4 TESTING THE ALGORITHM

Before applying the MEM algorithm to the real data, simulations were carried out to test its performance. Two-dimensional sky maps were simulated using a standard cold, dark matter model ($H_o = 50\mathrm{km\,s^{-1}}$, $\Omega_b = 0.1$) with an *rms* signal of 22μK per pixel (normalised to COBE second year data, $Q_{rms-PS} = 20.3\mu$K, see Tegmark & Bunn 1995). Observations from the sky maps were then simulated by convolving them with the Tenerife beam. Before noise was added the positive/negative algorithm was tested by analysing the data and then changing the sign of the data and reanalysing again. In both cases the same, but inverted, reconstruction was found for the MEM output and so we conclude that our method of two positive channels introduces no biases towards being positive or negative. Various noise levels were then added to the scans before reconstruction with MEM. The two noise levels considered here are 100μK and 25μK on the data scans, which represent the

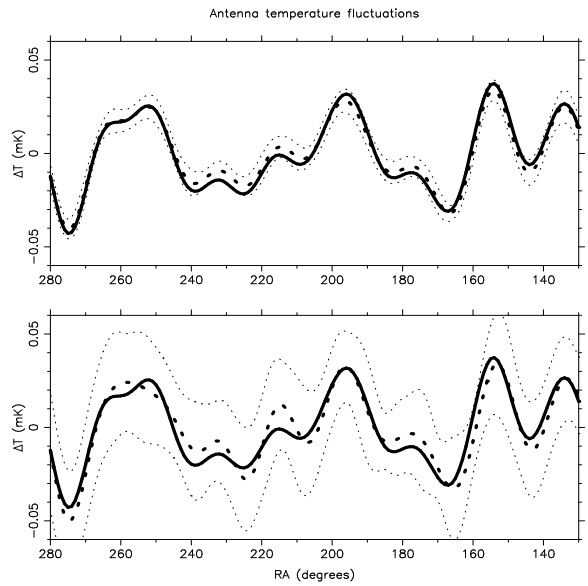

Figure 4. The solid line shows the sky simulation convolved with the Tenerife 8° experiment. The bold dotted line in the top figure shows the MEM reconstructed sky after reconvolution with the Tenerife beam, averaged over simulations of the MEM output from a simulated experiment with 25μK Gaussian noise added to each scan. Also shown are the 68% confidence limits (simulation to simulation variation; dotted lines) on this reconvolution. The bold dotted line in the bottom figure shows the reconvolution averaged over simulations with 100μK Gaussian noise added to each scan. The 68% confidence bounds (dotted lines) are also shown for this scan.

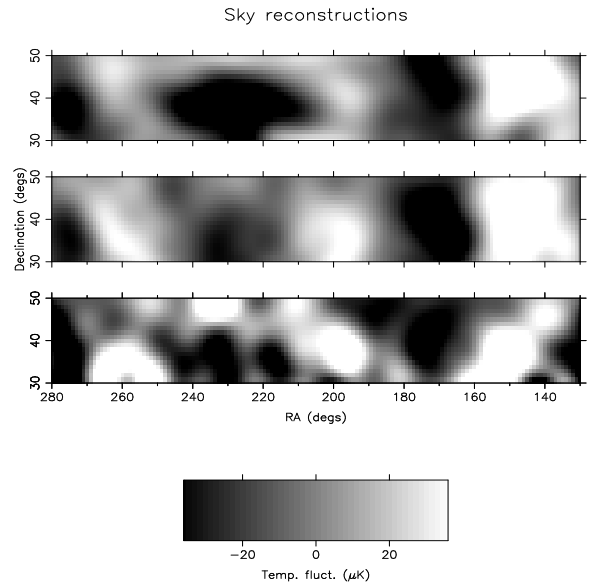

Figure 5. The top figure is the simulated sky convolved with an 8° Gaussian beam. The middle and bottom figures are the reconstructed skies from that simulation after scans with 25μK and 100μK noise levels respectively, simulating the Tenerife experiment, were made and passed through MEM. They are all convolved with a final Gaussian of the same size.

two extrema of the data that we expect from the various Tenerife configurations (100μK for the 10 GHz, FWHM=8° data and 25μK for the 15 and 33 GHz, FWHM=5° data).

Figure 4 shows the convolution of one simulation with the Tenerife beam and the result obtained from MEM with the two noise levels. The plots are averaged over 30 simulations and the bounds are the 68% confidence limits (simulation to simulation variation). As seen MEM recovers the underlying sky simulation to good accuracy for both noise levels, with the 25μK result the better of the two as expected. Figure 5 shows the reconstructed intrinsic sky from two of the simulations after 60 iterations of the MEM algorithm as compared with the real sky simulations convolved in an 8° Gaussian beam. Various common features are seen in the three scans like the maxima at RA 150°, minima at RA 170° and the partial ring feature between RA 200° and 260° with central minima at RA 230°, Dec. +35°. All features larger than the *rms* are reconstructed in both the 25μK and 100μK noise simulations. However, there is a some freedom in the algorithm to move these features within a beam width. This can cause spurious features to appear at the edge of the map when the guard region (about 5°) around the map contains a peak (this can be seen in the map as a decaying tail away from the edge). For example, the feature at RA 230°, Dec 50° has been moved down by a few degrees out of the guard region in the 100μK noise simulation so it appears more prominently on the ring feature.

There is a tendency for the MEM algorithm to produce superresolution (Narayan & Nityananda 1986) of the features in the sky so that even though the experiment may not be sensitive to small angular scales the final reconstruction appears to have these features in it. Care must be taken not to interpret these features as actual sky features but instead the maps should be convolved back down with a Gaussian to the size of the features that are detectable. This has been done with the two lower plots in Figure 5, so that a direct comparison between all three is possible. By comparison of these plots we are confident in saying that the reconstructed sky obtained from the MEM algorithm does give us a good description of the actual sky.

As an indicator of the error on the final sky reconstruction from the MEM, a histogram of the fractional difference between the input and output map temperatures is plotted in Figure 6. If the initial temperature at pixel (i, j) is given by T_{input} and the temperature at the same pixel in the output reconstructed map (after convolution with a Gaussian beam to avoid superresolution) is given by T_{recon} then the value of

$$\frac{\mathrm{T}_{recon} - \mathrm{T}_{input}}{\mathrm{T}_{input}} \tag{17}$$

is put into discrete bins and summed over all (i, j). The final histogram is the number of pixels within each bin. The output map has been averaged over pixels within the beam FWHM as features can move by this amount. A graph centred on -1 would mean that the amplitude of the output signal is near zero while a graph centred on 0 would mean the reconstruction is very accurate. As can be seen both graphs (Figure 6 (a) and (c) for the 25μK and 100μK noise simulations respectively) can be well approximated by a Gaussian centred on a value just below zero. This means that the MEM has a tendency to reconstruct the data with slightly smaller amplitude which increases with the level of noise ($\sim$ 10% smaller for the 25μK simulation and $\sim$ 20% for the 100μK simulation). This is expected from the entropy

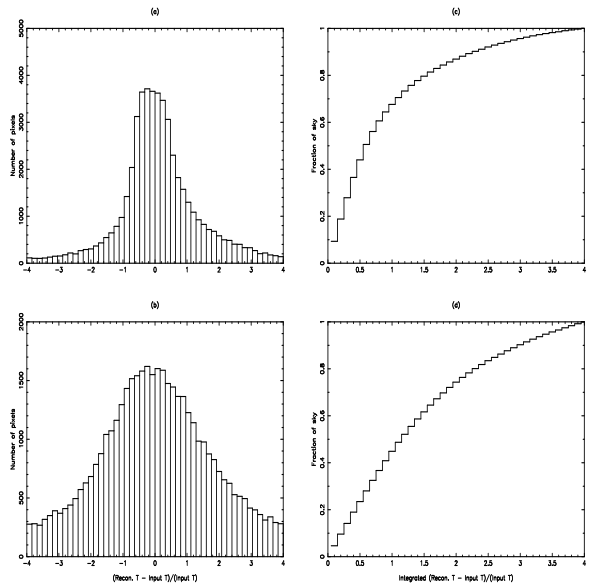

Figure 6. Histograms of the errors in the reconstruction of the simulated sky maps. (a) shows the $\frac{\mathrm{T}_{recon}-\mathrm{T}_{input}}{\mathrm{T}_{input}}$ for the 25μK noise simulation and (c) shows the integrated $\left|\frac{\mathrm{T}_{recon}-\mathrm{T}_{input}}{\mathrm{T}_{input}}\right|$ for (a). (b) and (d) are the corresponding plots for the 100μK noise simulation.

'damping' property. From the integrated plots (Figure 6 (b) and (d)) we can expect to reconstruct all features with better than 50% accuracy a half of the time for the 25μK noise simulation and a third of the time for the 100μK noise simulation. The next section describes the implementation of the algorithm for the actual 8° Tenerife experiment data.

5 RECONSTRUCTING THE SKY AT 10.4 GHZ

To apply the deconvolution process described in Section 2 to the data in Section 3 one must decide on the required dynamic range for the reconstruction and also select parameters that not only achieve convergence of the iterative scheme, but also make the fullest use of the data. The amplitude of the fluctuations that we are interested in is at least an order of magnitude smaller than the magnitude of the signal produced during the major passage through the Galactic plane region ($\sim$ 45 mK at $\sim$ Dec. +40°). Clearly, any baseline fitting and reconstruction will be dominated by this feature at the expense of introducing spurious features into the regions in which we are interested. For this reason the data (Table 3) corresponding to the principal Galactic plane crossing are not used in the reconstruction.

In contrast, the anti-centre crossing ($\sim$RA 60° at $\sim$Dec. +40°) corresponding to scanning through the Galactic plane, but looking out of the Galaxy, is at an acceptable level ($\lesssim$5 mK) and is a useful check on the performance and consistency of the observations. With the parameters set as in Table 2, χ^2 demonstrates a rapid convergence. For example, the change in χ^2 after 120 iterations of MEM is $\Delta\chi^2/\chi^2 \simeq -9\times10^{-4}$ while the change in χ^2_{base} is $\Delta\chi^2_{base}/\chi^2_{base} \simeq -2\times10^{-4}$.

The fitted baselines are subtracted from the raw data set to provide data free from baseline effects, allowing the scans for a given declination to be stacked together to provide a single high sensitivity scan. However, problems arise when the baseline variations in the raw data are so extreme as to prevent their successful removal in the MEM deconvolution analysis. As noted in Davies *et al.* (1996a), this problem is exaggerated at the higher frequencies where the water vapour emission is higher. At these higher frequencies it is clear that the variations in baseline are, in certain cases, too extreme for removal and will therefore result in artefacts in the final stacked scan. We are confident that these artefacts result from poor observing conditions rather than being intrinsic to the astronomy, because such problems occur only for days with severe baselines and appear in a randomly distributed fashion for different days. Removal of such data is essential if one is to obtain the necessary sensitivity to detect CMB fluctuations. This involves the laborious task of examining each raw scan and its baseline and deciding if the data are usable. In such cases where the data is un-salvageable, then the data for the full 360° observation are discarded. This ensures that there is no bias introduced by selectively removing features in the scans. After this final stage of editing, the baseline fitting must be repeated for the full remaining data set. The MEM process will now be able to search for a more accurate solution and will produce a new set of more accurate baselines. The coverages of a given declination can now be stacked together. Figure 7 shows the stacked results at each declination compared with the reconvolution of the MEM result with the beam. The main Galactic crossing has been excluded from this data but the weak Galactic crossing is clearly visible at RA=50°-100°. Only data points on the sky with more than ten independent measurements have been plotted and in the absence of data the continuity between declinations has clearly been used by the MEM to reconstruct the scans. At lower declinations this crossing shows a complex structure with peak amplitudes $\sim$ a few mK. The data with better sensitivities are those at Dec.=+39.4°and +1.1°.

The sky is not fully sampled with this data set but the MEM uses the continuity and 'damping' constraints on the data to reconstruct a two-dimensional sky model. In Figure 8, the sky reconstruction is shown. Although a rectangular projection has been used for display, the underlying computations use the full spherical geometry for the beams (as described in Section 3.2). The anti-centre crossings of the Galactic plane are clearly visible on the right hand side of

Table 3. The Galactic plane regions excised at each declination.

Declination	RA range excised (degrees)
+46.6°	275-340
+42.6°	275-340
+39.4°	275-340
+37.2°	275-340
+27.2°	280-320
+17.5°	265-310
+07.3°	255-310
+01.1°	255-310
−02.4°	260-310
−17.3°	255-300

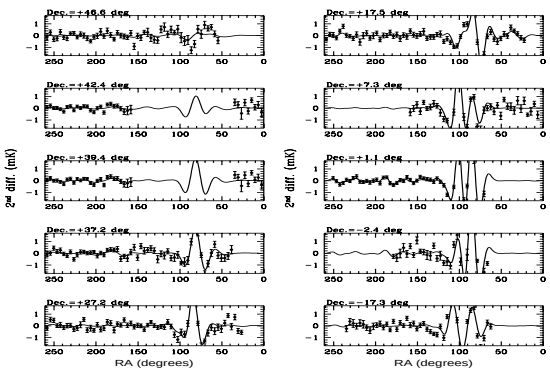

Figure 7. The stacked scans at each declination displayed as a function of right ascension. Again the plots are the second difference binned into 4° bins and the 68% confidence limits. The main Galactic plane crossing has been excluded, and only positions on the sky in which we have more than ∼10 independent measurements have been plotted. Also shown (solid line) is the reconvolved result from MEM overlayed onto each declination scan.

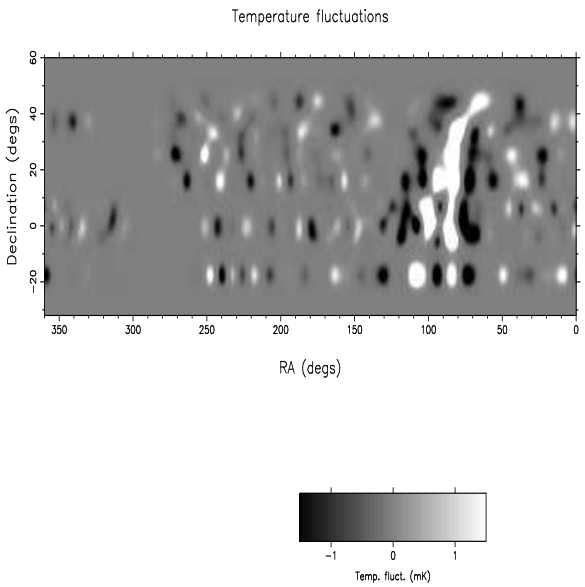

Figure 8. MEM reconstruction of the sky at 10.4 GHz, as seen by the Tenerife 8.4° FWHM experiment.

the image, while one should recall that the principal Galactic crossing has been excised from the data. It is clearly seen that there is apparent continuity of structure between adjacent independent data scans which are separated by less than the 8° beam width (see the higher declination strips in the plot where the data are more fully sampled). Where the data are not fully sampled (the lower declinations) the MEM has reverted to zero as expected and this is seen as 'stripping' along declinations in the reconstructed map.

In the next section we compare our reconstructed sky, reconvolved MEM scans and stacked data scans with the expected CMB and foreground signals at this observing frequency.

6 NON-COSMOLOGICAL FOREGROUND CONTRIBUTIONS

6.1 Point sources

We have estimated the contribution of discrete sources to the Tenerife 10 GHz data using the Kühr *et al.* (1981) catalogue, the VLA calibrator list and the Green Bank sky surveys (Condon & Broderick 1986); sources $\lesssim$1 Jy at 10.4 GHz were not included in the analysis. We have modelled the response of our instrument to these point sources by converting their fluxes into antenna temperature (1 Jy is equivalent to 12 μK for our experiment), convolving these with the triple beam of our instrument and sampling as for the real data (see the details in Gutiérrez *et al.* 1995). The two main radio sources at high Galactic latitude, which we expect to see in the Tenerife scans are 3C 273 (RA=$12^h26^m33^s$, Dec.=$+02°19'43''$) with a flux density at 10 GHz $\sim$ 45 Jy; this object should contribute with a peak amplitude $\Delta T \sim 500$ μK in the triple beam to our data at Dec.=+1.1°, and 3C84 (RA=$3^h16^m30^s$, Dec.=$+41°19'52''$) with a flux density at 10 GHz $\sim$ 51Jy. Figure 9 presents a comparison between our MEM result reconvolved in the Tenerife triple beam, the data and the predicted contribution of the radio source 3C273. We will show below how a diffuse Galactic contribution near the position of this point source accounts for the differences in amplitude and shape of the radio source prediction and our data. The radio sources 3C 273 and 3C84 have also been detected in the deconvolved map of the sky shown in Figure 8. For example, 3C 273 is seen with an amplitude of 1200 $\pm$ 140μK. Also clearly detected are 3C345 (RA=$16^h41^m18^s$, Dec.=$+39°54'11''$)and 4C39 (RA=$9^h23^m56^s$, Dec.=$+39°15'23''$) in both the reconvolved scans and the deconvolved map. Many other sources are seen in the deconvolved map but these may be swamped by the Galactic emission so we cannot say with confidence that any originate from point sources. These could originate from the diffuse Galactic emission or from the CMB. For example, features at Dec.∼+40°, RA∼180°, Dec.∼+17.5°, RA∼240°and Dec.∼+1.1, RA∼ 220° do not correspond to any known radio sources (see Figure 7). The additional contribution by unresolved radio sources has been estimated to be $\Delta T/T \sim 10^{-5}$ at 10.4 GHz (Franceschini *et al.* 1989) in a single beam, and so will be less in the Tenerife switched beam, and is not considered in the analysis presented here.

6.2 Diffuse Galactic contamination

The contribution of the diffuse Galactic emission in our data can be estimated in principle using the available maps at frequencies below 1.5 GHz. We have used the 408 MHz (Haslam *et al.* 1982) and 1420 MHz (Reich & Reich 1988) surveys; unfortunately the usefulness of these maps is limited because a significant part of the high Galactic latitude structure evident in them is due to systematic effects (Davies, Watson & Gutiérrez 1996b). Only in regions (such as crossings of the Galactic plane) where the signal dominates clearly over the systematic uncertainties, is it possible to estimate the expected signals at higher frequencies. With this in mind, we have converted these two maps to a common resolution (1°x 1°in right ascension and declination respectively) and convolved them with our triple beam response.

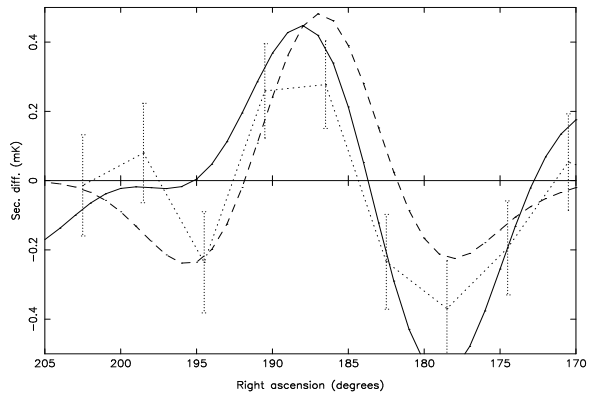

Figure 9. Comparison between the MEM reconstructed sky convolved in the Tenerife beam (solid line), the predicted point source contribution at Dec.=1.1° (dashed line) and the Tenerife data (dotted line with one sigma error bars shown). The source observed is 3C273 (RA= $12^h 26^m 33^s$, Dec.= $+02°19'43''$).

We can compare this contribution at 408 and 1420 MHz, with our data at 10.4 GHz to determine the spectral index of the Galactic emission in the region where these signals are high enough to dominate over the systematic effects in the low frequency surveys. We assume a power law spectra ($T \propto \nu^{-\beta}$) for the signal with an index independent of the frequency, but varying spatially. The signals in the Galactic anti-centre are weaker than those for the Galactic plane crossing and are mixed up with several extended structures, but even in this case we can draw some conclusions about the spectral index in this region; we obtain $\beta = 3.0 \pm 0.2$ between 408/1420 MHz and $\beta = 2.1 \pm 0.4$ between 1420/10400 MHz which indicates that free-free emission dominates over synchrotron at frequencies $\gtrsim$1420 MHz. One of the stronger structures in the region away from the galactic plane is in RA$\sim$ $12^h - 13^h$, Dec$\sim$ 0° and therefore the main contribution should be to our data at Dec=1.1°. This structure at 408 MHz, assuming an spectral index $\beta = 2.8$, gives a predicted peak amplitude at 10.4 GHz of $\sim$ 500 μK; we believe that this is responsible for the distortion between our measurements at Dec=1.1°and the predictions for the radio source 3C 273.

7 STATISTICAL ANALYSIS

We have analysed the statistical properties of the signals present in our data using the likelihood function and a Bayesian analysis. This method has been widely used in the past by our group (see *e.g.* Davies *et al.* 1987) and incorporates all the relevant parameters of the observations: experimental configuration, sampling, correlation between measurements, etc. The analysis assumes that both the noise and the signal follow a Gaussian distribution fully determined by their respective auto-correlation function (ACF). The source of dominant noise in our data is thermal noise in the receivers which is independent in each data-point (Davies *et al.* 1996a) and therefore it only contributes to the terms in the diagonal of the ACF matrix. We have restricted our analysis to data in which we have a minimum number of 10 independent measurements for the full RA range (Dec. 7.3° does not have enough data) and to data

Table 4. Statistics of the data used in the analysis. 95% confidence limits are shown.

Dec.	RA	σ (μK)	Indep.	$(\frac{l(l+1)}{2\pi}C_l)^{1/2}$ (10^{-5}) (μK)
+46.6°	161°-250°	116	15	≤ 8.5
+42.6°	161°-250°	117	14	≤ 10.3
+39.4°	176°-250°	81	42	$1.8^{+2.3}_{-2.0}$
+37.2°	161°-250°	113	17	$5.7^{+3.2}_{-2.9}$
+27.2°	161°-240°	139	11	$4.5^{+3.0}_{-3.9}$
+17.5°	171°-240°	144	12	$4.3^{+3.0}_{-4.4}$
+1.1°	171°-230°	96	58	$5.0^{+3.3}_{-3.0}$

for which we have a point source prediction (Dec. $-17.3°$ is not covered by the Green Bank survey). This region represents approximately 3000 square degrees on the sky. Table 4 presents the sensitivity per beam in the RA range used in this analysis. Also column 4 gives the mean number of independent measurements which contribute to each point. We emphasize that this statistical analysis has been performed directly on the scan data, and not on the MEM deconvolved sky map produced during the baseline subtraction process. Thus, for this section, any effects of using a MEM approach are restricted to the baselines subracted from the raw data, which will not contain or affect any of the astronomical information to which the likelihood analysis is sensitive.

We made two different analyses: the first considers the data of each declination independently, and the second considers the full two-dimensional data set for the analysis. Due to the spherical nature of the sky we expand the fluctuations using spherical harmonics Y_l^m (see for example Efstathiou 1989),

$$\frac{\Delta T}{T}(\theta,\phi) = \sum_{l,m} a_l^m Y_l^m(\theta,\phi). \tag{18}$$

A likelihood analysis was performed assuming a Harrison-Zel'dovich spectrum, thus the parameter fitted for was the cosmic quadrupole normalisation for the spherical harmonic expansion, Q_{RMS-PS} (see Smoot *et al.* 1992). Since the l range sampled is small we can easily get an equivalent flat band pass estimate for C_l ($C_l =< |a_l^m|^2 >$) and this is what is shown in the Table 4. The experiment has a peak sensitivity to an l of about 12. The fifth column of Table 4 gives, for the one-dimensional analysis, the amplitude of the signal detected with the one-sigma confidence level. The confidence limits on these signals were found by integration over a uniform prior for the likelihood function. These analyses ignore correlations between measurements at adjacent declinations. Therefore a full likelihood analysis, taking this correlation into account, should constrain the signal more efficiently. It should be noted that the two dimensional analysis assumes that the signal has the same origin over the full sky coverage but this may not be the case because of the differing levels of Galactic signal between declinations and across the RA range. In Figure 10 the likelihood function resulting from this analysis is shown. It shows a clear, well defined peak at $(\frac{l(l+1)}{2\pi}C_l)^{1/2}$ $(10^{-5}) = 2.6^{+1.3}_{-1.6}$ (95 % confidence level). This value would correspond to a value of $Q_{RMS-PS} = 45.2^{+23.8}_{-27.2}$ μK. Our results are compatible with the constraints on the signal in each declination considered separately but it is clear that the two dimensional likelihood analysis improves the constraints on the amplitude of the astronomical signal.

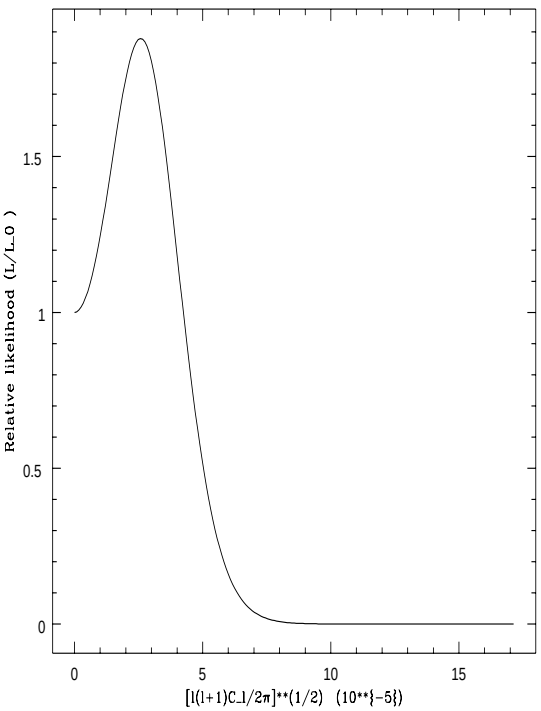

Figure 10. The likelihood function from the analysis of the full data set. There is a clearly defined peak at $(\frac{l(l+1)}{2\pi}C_l)^{1/2}\,(10^{-5}) = 2.6^{+1.3}_{-1.6}$ (95% confidence level).

We may compare the results obtained here with the amplitude of the CMB structure found in Hancock *et al.* (1994) at higher frequencies. They found $Q_{RMS-PS} \sim 21\mu$K in an 5° FWHM switched beam and taking into account the extra dilution we expect a slightly lower level in an 8° FWHM switched beam, assuming a $n = 1$ power spectrum. We thus see that it is likely that the majority of the signal in the 10 GHz, FWHM=8 deg data is due to Galactic sources. If we assume that the majority of the signal found here is Galactic synchrotron or free–free and we use a spatial spectrum of $C_l \propto l^{-3}$ (estimated from the Haslam *et al.* 1982 maps) to predict the expected galactic contamination in a 5° FWHM beam at 10 GHz, then using a full likelihood analysis we find that we expect an *rms* temperature across the scans of $\Delta T_{rms} = 55^{+32}_{-26}$ μK. We note that this is an upper limit on the Galactic contribution to the 5° data as the variability of the sources has been ignored when the subtraction was performed (this results in a residual signal from the point sources in the data during the likelihood analysis) and the analysis also includes regions where the Galactic signal is expected to be higher (for example the North Polar Spur). The 5° FWHM Tenerife scans are centred on Dec. 40° and it can be seen from Table 4 that this is the region with the lowest Galactic contamination. The results reported in Gutierrez *et al* (1997), for the 5° FWHM, 10 GHz Tenerife experiment, show that the signal found was $Q_{RMS-PS} < 33.8$ μK (corresponding to a signal of $\Delta T_{rms} < 53$ μK) which is consistent with our prediction (also taking into account the more significant contribution from the CMB at 5 deg). This comparison allows us to restrict the *maximum* Galactic contribution to the signal found in Hancock *et al.* 1994 to be $\Delta T_{rms} \sim 18 - 23\mu$K at 15 GHz and $\Delta T_{rms} \sim 2 - 4\mu$K at 33 GHz depending on whether the contamination is dominated by synchrotron or free-free emission.

8 CONCLUSIONS

We have presented here a new method for analysing the data from microwave background experiments. As seen from simulations performed in Section 4, the positive/negative MEM algorithm performs very well recovering the amplitude, position and morphology of structures in both the reconvolved scans and the two-dimensional deconvolved sky map. We conclude that no bias, other than the 'damping' enforcement, is introduced into the results from the methods described here, as the bare minimum of prior knowledge of the sky is required. A simultaneous baseline fit is also possible. Even with the lowest signal to noise ratio (the 100μK noise simulation which corresponds to our worse case in the Tenerife experiments) all of the main features on the sky were reconstructed. Using this method we are able to put constraints on the galactic contamination for other experiments at higher frequencies which is essential when trying to determine the level of CMB fluctuations present.

It is clear that this approach works well and provides a useful technique for extracting the optimum CMB maps from both current and future multi-frequency experiments. This will become of ever increasing importance as the quality of CMB experiments improves. At present we are using this method to analyse the new data from the three beam switching Tenerife experiments at 10 GHz, 15 GHz and 33 GHz with angular resolutions of $\sim 5^\circ$. We hope the two dimensional results from these will be available shortly.

ACKNOWLEDGEMENTS

The Tenerife experiments are supported by the UK Particle Physics and Astronomy Research Council, the European Community Science programme contract SCI-ST920830, the Human Capital and Mobility contract CHRXCT920079 and the Spanish DGICYT science programme. A.W. Jones wishes to acknowledge a UK Particle Physics and Astronomy Research Council Studentship. S. Hancock wishes to acknowledge a Research Fellowship at St. John's College, Cambridge, UK. G. Rocha wishes to acknowledge a JNICT Studentship from Portugal.

REFERENCES

Bunn, E.F., Hoffman, Y., & Silk, J. 1996, ApJ, 464, 1
Condon, J.J., & Broderick, J.J. 1986, AJ, 91, 1051
Davies, R.D. Lasenby, A.N., Watson, R.A., Daintree, E.J., Hopkins, J., Beckman, J., Sanchez-Almeida, J. & Rebolo, R. 1987, Nature, 326, 462
Davies, R.D., Watson, R.A., Daintree, E.J., Hopkins, J., Lasenby, A.N., Sanchez-Almeida, J., Beckman, J.E. & Rebolo, R. 1992, MNRAS, 258, 605
Davies, R.D. *et al.* 1996a, MNRAS, 278, 883
Davies, R.D., Watson, R.A., & Gutiérrez, C.M. 1996b, MNRAS, 278, 925

Efstathiou, G. 1989, in 'Physics of the early universe', proc. 36th Scottish Uni. Summer School, Adam Hilger, New York, ed. Peacock, J.A., Heavens, A.F. & Davies, A.T.
Franceschini, A., Toffolatti, L., Danese, L., & De Zotti, G. 1989, ApJ, 344, 35
Gull, S.F. 1989 Maximum Entropy and Bayesian Methods, 53, ed. J. Skilling
Gutierrez de la Cruz, C. M., Davies, R. D., Rebolo, R., Watson, R. A., Hancock, S., & Lasenby, A. N. 1995, ApJ, 442, 10
Gutierrez, C. M., Hancock, S., Davies, R. D., Rebolo, R., Watson, R. A., Hoyland, R.J., Lasenby, A. N. & Jones A.W. 1997, ApJ, 480, L83
Hancock, S. et al. 1994, Nature, 367, 333
Haslam, C.G.T., Salter, C.J., Stoffel, H., & Wilson, W.E. 1982, A&AS, 47, 1
Kühr, H., Witzel, A., Pauliny-Toth, I.I.K., & Nauber, U. 1981, A&AS, 45, 367
Laue, E., Skilling J., & Staunton J. 1985, J. Mag. Res, 63, 418
Maisinger, K., Hobson, M.P. & Lasenby, A.N. 1997, MNRAS, in press
Narayan, R., & Nityananda, R. 1986, Ann. Rev. Astron. Astrophys., 24, 127
Reich, P., & Reich, W. 1988, A&AS, 74, 7
Skilling, J. 1989, Maximum Entropy and Bayesian Methods, 45, ed. J. Skilling
Smoot, G.F. et al. 1992, ApJ, 396, L1
Tegmark, M., & Bunn, E.F., 1995, ApJ, 455, 1
Watson, R.A., DeLaCruz, C.M.G., Davies, R.D., Lasenby, A.N., Rebolo, R., Beckman, J.E. & Hancock S. 1992, Nature, 357, 660
White, M., & Bunn, E. 1995, ApJ, 443, L53

Figure captions

Figure 1: The 15 scans obtained at Dec = 46.6° displayed as a function of right ascension. Each plot shows the second difference in mK after binning into 1° bins. A running mean has been subtracted from each scan. Long scans are displayed modulo 360°.

Figure 2: The data from scan 5 of Figure 1 displayed on an expanded temperature scale against RA bin number. Long timescale variations in the mean level are evident in the RAW scan (bottom panel). The middle panel shows the baseline fit found by the method of Section 2. The top panel shows the baseline corrected scan. The bin numbers exceed 360 since the scan begins near the end of an LST day, and the data are not folded modulo 360°.

Figure 3: The transfer function for the Tenerife experiments.

Figure 4: The solid line shows the sky simulation convolved with the Tenerife 8° experiment. The bold dotted line in the top figure shows the MEM reconstructed sky after reconvolution with the Tenerife beam, averaged over simulations of the MEM output from a simulated experiment with 25μK Gaussian noise added to each scan. Also shown are the 68% confidence limits (dotted lines) on this reconvolution. The bold dotted line in the bottom figure shows the reconvolution averaged over simulations with 100μK Gaussian noise added to each scan. The 68% confidence bounds (dotted lines) are also shown for this scan.

Figure 5: The top figure is the simulated sky convolved with an 8° Gaussian beam. The middle and bottom figures are the reconstructed skies from that simulation after scans with 25μK and 100μK noise levels respectively, simulating the Tenerife experiment, were made and passed through MEM. They are all convolved with a final Gaussian of the same size.

Figure 6: Histograms of the errors in the reconstruction of the simulated sky maps. (a) shows the $\frac{\mathrm{T}_{recon}-\mathrm{T}_{input}}{\mathrm{T}_{input}}$ for the 25μK noise simulation and (c) shows the integrated $\left|\frac{\mathrm{T}_{recon}-\mathrm{T}_{input}}{\mathrm{T}_{input}}\right|$ for (a). (b) and (d) are the corresponding plots for the 100μK noise simulation.

Figure 7: The stacked scans at each declination displayed as a function of right ascension. Again the plots are the second difference binned into 4° bins and the 68% confidence limits. The main Galactic plane crossing has been excluded, and only positions on the sky in which we have more than ∼10 independent measurements have been plotted. Also shown (solid line) is the reconvolved result from MEM overlayed onto each declination scan.

Figure 8: MEM reconstruction of the sky at 10.4 GHz, as seen by the Tenerife 8.4° FWHM experiment.

Figure 9: Comparison between the MEM reconstructed sky convolved in the Tenerife beam (solid line), the predicted point source contribution at Dec.=1.1° (dashed line) and the Tenerife data (dotted line with one sigma error bars shown). The source observed is 3C273 (RA= $12^h26^m33^s$, Dec.= $+02°19'43''$).

Figure 10: The likelihood function from the analysis of the full data set. There is a clearly defined peak at $(\frac{l(l+1)}{2\pi}C_l)^{1/2}\,(10^{-5}) = 2.6^{+1.3}_{-1.6}$ (95% confidence level).